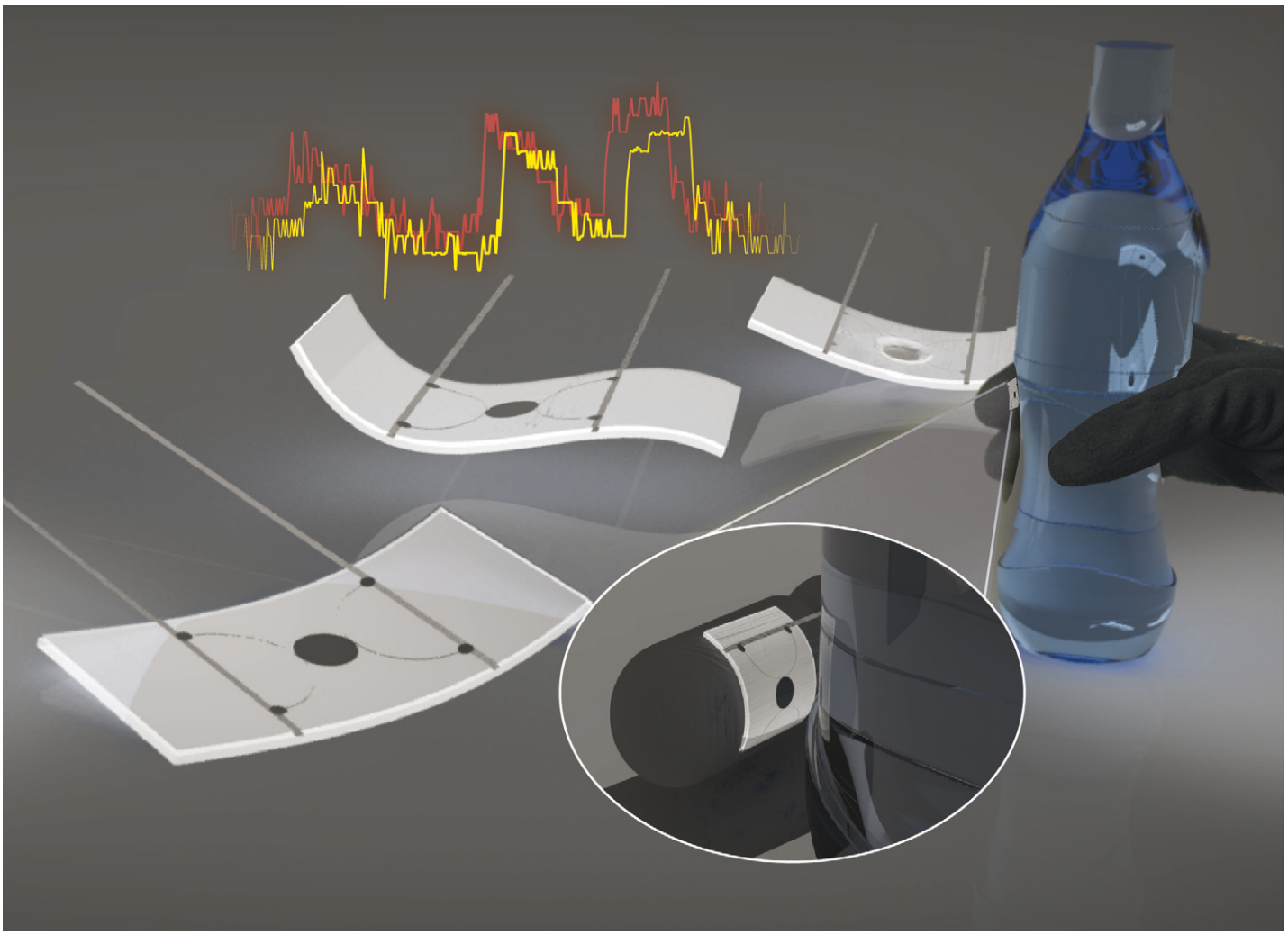

Featuring work from the group of Professor Chwee Teck Lim at the Department of Biomedical Engineering, National University of Singapore.

Wearable tactile sensor based on flexible microfluidics

A facile method of fabricating wearable tactile sensors was demonstrated. The sensors are thin, flexible, robust and sensitive enough to be mounted on the skin or embedded in a glove to measure tactile forces.

As featured in:

See Chwee Teck Lim *et al.*, *Lab Chip*, 2016, **16**, 3244.

ROYAL SOCIETY OF CHEMISTRY

www.rsc.org/loc

Registered charity number: 207890

Lab on a Chip

PAPER

View Article Online
View Journal | View Issue

Cite this: *Lab Chip*, 2016, **16**, 3244

Wearable tactile sensor based on flexible microfluidics†

Joo Chuan Yeo,[abc] Jiahao Yu,[b] Zhao Ming Koh,[b] Zhiping Wang[a] and Chwee Teck Lim*[bc]

Received 30th April 2016,
Accepted 7th July 2016

DOI: 10.1039/c6lc00579a

www.rsc.org/loc

In this work, we develop a liquid-based thin film microfluidic tactile sensor of high flexibility, robustness and sensitivity. The microfluidic elastomeric structure comprises a pressure sensitive region and parallel arcs that interface with screen-printed electrodes. The microfluidic sensor is functionalized with a highly conductive metallic liquid, eutectic gallium indium (eGaIn). Microdeformation on the pressure sensor results in fluid displacement which corresponds to a change in electrical resistance. By emulating parallel electrical circuitry in our microchannel design, we reduced the overall electrical resistance of the sensor, therefore enhancing its device sensitivity. Correspondingly, we report a device workable within a range of 4 to 100 kPa and sensitivity of up to 0.05 kPa^{-1}. We further demonstrate its robustness in withstanding >2500 repeated loading and unloading cycles. Finally, as a proof of concept, we demonstrate that the sensors may be multiplexed to detect forces at multiple regions of the hand. In particular, our sensors registered unique electronic signatures in object grasping, which could provide better assessment of finger dexterity.

Introduction

Physical sensors, such as pressure sensors and strain gauges, are fundamental elements across various industry sectors, such as healthcare,[1–3] consumer electronics,[4,5] robotics,[6,7] and manufacturing. Among these, sensors for health monitoring are gaining popularity due to the trend of Internet of Things (IoT) which enables strong network connectivity between physical objects and their users. Therefore, these sensors are found in diverse applications, such as in fitness tracking,[8,9] rehabilitation,[10–12] disease monitoring,[13] and wound healing.[14] However, stringent demands are required for sensors to monitor human activity in their natural environment. Fundamentally, these wearable sensors should be imperceptible, non-obtrusive and yet of high reliability. Therefore, in the physical aspect, the sensors need to be flexible, bendable, lightweight and deformable to match the mechanical properties of the human skin. However, sensors relying on piezoelectric silicon-based materials fail to meet these requirements, since conventional photolithographic fabrication methods utilize rigid substrates that limit deformability.

To overcome these challenges, recent research on flexible tactile or pressure sensors focuses on conductive materials using PEDOT:PSS,[15] carbon nanotubes,[8,16,17] metallic nanowires,[4,10] novel 2D materials,[18–20] or conductive fluids.[21,22] Among these, conductive liquids, such as eutectic gallium indium (eGaIn) and Gallistan, present a unique proposition because they are highly conductive, non-viscous and chemically inert.[23] Furthermore, they are stable over a wide range of temperatures, making them easy to implement on polymeric substrates. However, they are generally expensive due to the use of rare earth metals. Microfluidics thus presents a compelling case for the use of conductive liquids as it requires only minute amounts and physical forces are accentuated within these micro-conduits. In our previous study, we have demonstrated the use of a eGaIn-based microfluidic tactile sensor to measure localized foot pressure.[24] Even so, the microchannel leads to unnecessarily high resistance which affects its pressure sensitivity.

Moreover, wearable sensors are required to be functional over a wide range of forces with high durability and sensitivity. In particular, mechanoreceptors in our fingers are able to perceive pressures as low as 4 kPa.[25] Yet, our daily activities involve many activities such as keyboard typing or object grasping that covers a wide range of pressures to over 200 kPa. Furthermore, pressure changes as low as 2 kPa may be perceived by our fingers.[26] Here, few pressure sensors are able to fall within the limits of both parameters. Typically, sensors showed remarkably high sensitivity only over low pressures below 10 kPa. For example, Zhu *et al.* developed a

[a] *Singapore Institute of Manufacturing Technology, A*STAR, 138634 Singapore*
[b] *Department of Biomedical Engineering, National University of Singapore, 117575 Singapore*
[c] *Mechanobiology Institute, National University of Singapore, 117411 Singapore. E-mail: ctlim@nus.edu.sg*

† Electronic supplementary information (ESI) available: Calculation of deformation mechanics. See DOI: 10.1039/c6lc00579a

microstructured PDMS layer deposited with graphene to achieve 5.53 kPa^{-1} for pressures below 100 Pa.[20] Similarly, Nie *et al.* developed a microdroplet array pressure sensing film of pressure sensitivity 77.7 pF kPa^{-1} over a range of 33 Pa to around 7 kPa.[21] Other researchers have demonstrated a wider pressure range with reduced sensitivity. For example, Gerratt *et al.* developed an elastomeric capacitive pressure sensor that was able to measure 10 kPa to 405 kPa with a pressure sensitivity of 0.001 kPa^{-1}.[27]

Here, we employed eGaIn because of its excellent electrical conductivity and physicochemical stability. We devised a microfluidic manifold comprising elastomeric rubber and polyethylene terephthalate (PET) film screen-printed with conductive electrodes. In particular, we developed microfluidic channels that are analogous to parallel electrical circuitry, thereby reducing the overall electrical resistance of the circuitry and improving its sensitivity. The sensors were attached to a customized WiFi module, allowing simultaneous data transmission at 10 Hz.

Results and discussion

Materials and methods

Device design and fabrication. The schematic of the microfluidic pressure sensor is presented in Fig. 1a. The microfluidic pressure sensor comprises a thin layer of micropatterned silicone elastomer (Ecoflex 0050, Smooth-On, Easton, Pennsylvania) and a PET film of 50 μm thickness (Zephyr Silkscreen Pte. Ltd., Singapore) screen-printed with conductive electrodes. The design of the microstructure consists of a central circular region with a diameter of 5 mm, four side circular regions with a diameter of 2.5 mm, and four arcs with a curvature radius of 6 mm and a channel width of 100 μm connecting the side circular regions to the central circular regions. The microstructure has a height of 80 μm. The thickness of the entire manifold measures approximately 2 mm. The fabrication process of the microfluidic pressure sensor is presented in Fig. 1b. Briefly, the master mold for the Ecoflex silicone rubber substrate was fabricated from the SU-8 photoresist on a silicon wafer based on the standard soft lithography technique. The soft silicone rubber, approximately 4 g, was mixed in a 1 : 1 base-to-hardener (w/w) ratio and poured directly onto the silanized wafer. It was then left at 70 °C for 1 h before it was carefully peeled off from the master mold to form the top layer of the sensor. Subsequently, the top layer of the silicone rubber and the bottom layer of the PET film were subjected to 5 min UV ozone treatment and brought together immediately. The assembly was left in the oven at 70 °C for another 2 h. The surface modification and thermal treatment resulted in an irreversible covalent bond between the two layers. Next, a liquid metallic alloy, *i.e.*, eGaIn, was introduced into the microstructure with a needle syringe. Finally, the fluidic ports of the microstructure were sealed using a thin layer of uncured silicone rubber to produce the final working pressure sensor. Fig. 1c shows the actual fabricated sensor. Owing to the softness of the silicone elastomer (Shore Hardness 50A), a small mechanical force can lead to deformation. This resulted in displacement of the conductive fluid beyond the electrodes. Fig. 1d shows the fabricated sensor when pressed with a needle. When the force is removed, the conductive fluid returns to its original state to fill up the displaced volume.

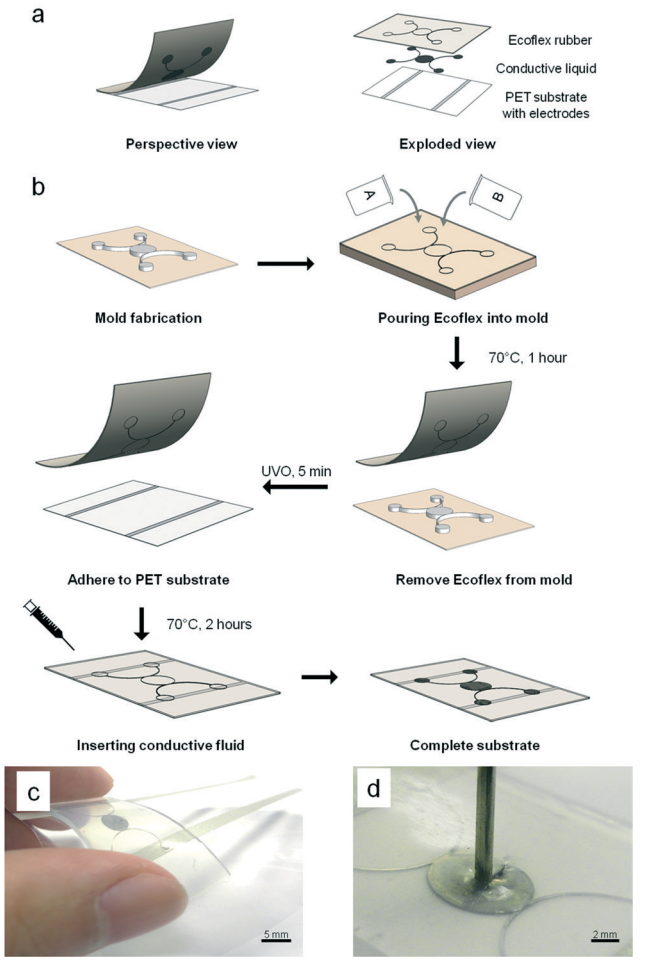

Fig. 1 Flexible microfluidic pressure sensor. (a) Perspective view and exploded view of the flexible microfluidic pressure sensor, respectively, comprising the conductive fluid sandwiched in between a thin layer of micropatterned silicone elastomer and a PET film screen-printed with silver electrodes. (b) Fabrication process of the flexible microfluidic pressure sensor. (c) Actual fabricated liquid-based microfluidic pressure sensor. (d) Macro views of the pressure sensor pressed by a needle.

Finite element modelling. Finite element modeling of the microfluidic pressure sensors was performed in SolidWorks Simulation and further processed in MATLAB. Four node shell elements were used for the silicone rubber substrate of density 1070 kg m^{-3}. The sensor was modeled as a viscoelastic material, with a compressive modulus of 209 kPa for pressures below 50 kPa and a compressive modulus of 1 MPa for pressures above 50 kPa. Boundary conditions were fixed at the bottom of the substrate.

Characterization of pressure sensor. The liquid-based microfluidic pressure sensor was subjected to compressive

ramp-hold-release loads starting from 4 kPa to 100 kPa over a contact diameter of 5 mm using a universal load machine (5848 MicroTester, Instron, Norwood, MA). The ramp and release rates were set at 5 mm min^{-1} and the hold duration was set at 30 s for static load evaluations. The electrical response of the pressure sensor upon different load applications was constantly monitored and recorded at 3 Hz using a custom-made digital potentiometer with a data logging function. For durability testing, the pressure sensor was mounted on a custom-made linear actuator system and subjected to loading–unloading cycles of approximately 10 kPa at 0.2 Hz for over 2500 cycles. For temperature variation testing, the pressure sensor was mounted on a custom-made electric heating plate. Ice packs were placed directly on the pressure sensor to reduce the temperature to 15 °C. The ice packs were then removed and the electrical heater was switched on. The temperature was recorded using a temperature logger (Extech Instruments, Nashua, NH).

Device working principle

The micropatterned silicone elastomer works similar to a micropump system, as illustrated in Fig. 2a. In particular, when the load is applied to the pressure sensing region, the microchannel collapses under the force, causing the fluid to be displaced to the end regions. Due to the change in cross-sectional area, the overall resistance of the pressure sensor is increased. The electrical resistance may be expressed in correlation with the silicone elastomer resembling mechanical beam acting on the conductive fluid. Assuming a uniform pressure P acting on the circular surface, the normalized electrical resistance, $\Delta R/R_0$, of the pressure sensor can be simplified by eqn (1),

$$\frac{\Delta R}{R_0} = \frac{2Pw}{(2w+d)(E_c - P)} \quad (1)$$

where E_c is the compressive modulus of the silicone elastomer, w is the width of the microfluidic channel, and d is the curvature diameter of the microchannel (see the ESI† for details). Intuitively, a low compressive modulus will be ideal for sensitivity. Furthermore, the diameter of the microchannel defines the loading capacity of the pressure sensor. Thus, the ideal material selection of the flexible pressure with defined height and width will provide precise and sensitive localized pressure sensing regions for different applications. Subsequently, when the load is removed, the pressure accumulated at the end regions pushes the fluid back to the pressure sensing region, resulting in its resistance to return to its baseline. The conductive fluid within the microchannels forms an electrically conductive path, similar to a conductive wire. The design of the micropatterned silicone elastomer could be depicted in an electrical circuitry diagram, as presented in Fig. 2b. Here, we utilized the parallel electrical circuitry phenomenon and reduced the effective electrical resistance of the sensor to approximately 3 Ω, which is 300% lower than that of series electrical circuitry. As device sensitivity, S, is described based on the normalized electrical resistance (*i.e.*, $S = \Delta R/R_0$, where R_0 is the electrical resistance baseline), the device sensitivity is thus enhanced with a lower baseline resistance.

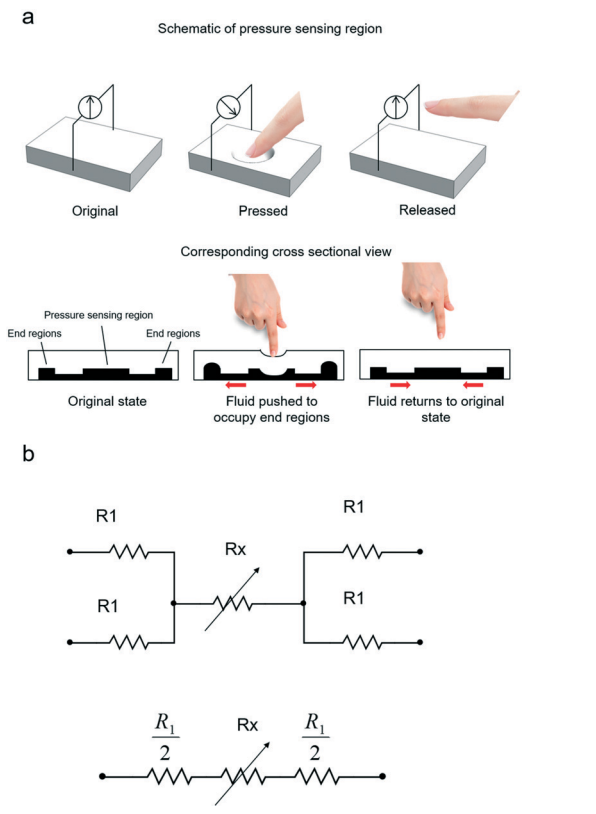

Fig. 2 Flexible microfluidic pressure sensor. (a) Working principle as a micropump system when the load is applied and removed, respectively. (b) Principle of operation illustrated using an electrical circuitry analogy.

Characterization of pressure sensor

To assess the sensitivity of the pressure sensor, we simulated localized loads between 2 kPa and 100 kPa over the entire pressure sensing region (*i.e.* contact diameter of 5 mm). As illustrated in Fig. 3a, the pressure is mainly confined within the pressure sensing region due to the material properties of the elastomer being soft and easily compressible. Fig. 3b further describes the deformation profile of the silicone elastomer in three dimensions, assuming a material thickness of 2 mm. When we compared the deformation profile due to the pressure load between 2 kPa and 50 kPa, we observed significant deformation with increasing pressure. Fig. 3c further quantifies the stress profile of the silicone elastomer over a range of loads from 2 kPa to 100 kPa (*i.e.* 2, 10, 15, 25, 50, 65, 75, 100 kPa). As shown, the stress region is the highest at the center of the pressure sensing region and decreases away from its axis. Furthermore, the stress increases proportionately with increasing pressure. Similarly, we also observed the deformation profile of the pressure sensing region over the

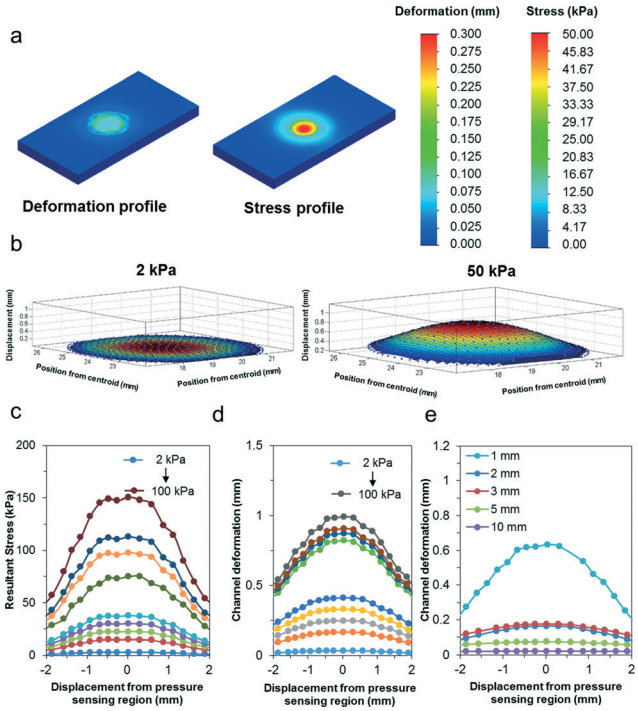

Fig. 3 Finite element modeling of the microfluidic pressure sensor. (a) Perspective view of the pressure sensor with a localized load of 50 kPa over the pressure region in relation to its deformation and stress, respectively. (b) Comparison of the deformation profile of the pressure sensing region with 2 kPa and 50 kPa, respectively. (c) Stress profile of the pressure over a range of loads, *i.e.* 2, 10, 15, 20, 25, 50, 65 75, 100 kPa. (d) Deformation profile of the pressure sensor over a range of loads, *i.e.* 2, 10, 15, 20, 25, 50, 65, 75, 100 kPa. (e) Deformation profile showing the effects of localized pressure (*i.e.* 10 kPa) over a range of thicknesses of the pressure sensing region, *i.e.* 1, 2, 3, 5, 10 mm.

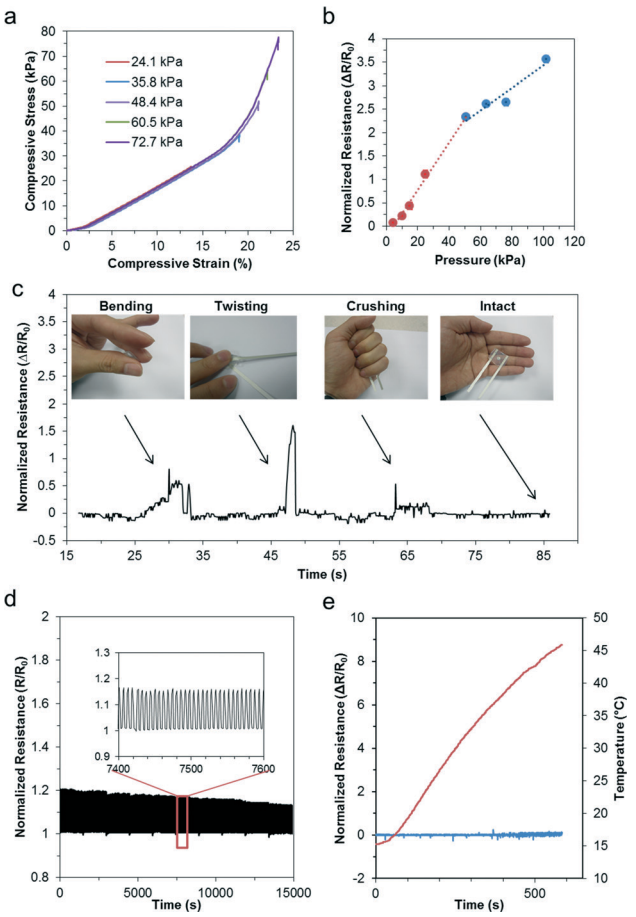

Fig. 4 Characterization of the microfluidic pressure sensor. (a) Material properties of the silicone elastomer upon compression. (b) Normalized electrical resistance change ($\Delta R/R_0$) profile of the pressure sensor over various pressure loads between 4 kPa and 100 kPa. (c) Normalized electrical resistance profile of the pressure sensor subjected to extreme deformations: bending, twisting, and crushing. (d) R/R_0 profile of the pressure sensor being subjected to 2500 loading–unloading cycles. The inset shows the magnification of the normalized resistance across a 200 s time span. (e) $\Delta R/R_0$ profile of the pressure sensor with respect to temperature between 15 °C and 45 °C.

same simulated loads. In Fig. 3d, the deformation profile of the micropatterned silicone elastomer is described quantitatively over the same applied loads. Notably, even a small pressure of 2 kPa translates to relatively large deformation of over 20 μm. Therefore, it indicates that our flexible pressure sensor possesses high localized sensitivity. Furthermore, when the simulated localized loads increase beyond 50 kPa, we observed nonlinear mechanical deformations due to the viscoelastic nature of the material. Finally, we simulated the effects of a localized pressure of 10 kPa over a range of thicknesses of the pressure sensor (*i.e.* 1, 2, 3, 5, 10 mm). Fig. 3e shows the deformation profile across the cross section of the pressure sensing region. With increasing thickness, the material is stiffer and subject to poorer deformations. Therefore, the pressure range and sensitivity can be altered based on the sensor thickness for different applications.

Next, we characterized the pressure sensing performance of the flexible pressure sensor using a universal loading machine. Static loads were performed under compressive ramp-hold-release load cycles on the device, starting from a pressure of 25.4 kPa up to 76.4 kPa. Fig. 4a shows the stress–strain curve of the silicone elastomer under the applied pressures. Based on this characterization, we determined the material properties of the silicone elastomer. Particularly, we noted that pressure within 48 kPa exhibited a fairly linear stress–strain relation with a low compressive modulus of 209 kPa. Evidently, a force as small as 18 kPa can result in a compressive strain of approximately 10%, highlighting its sensitivity. Furthermore, we also observed that at incremental pressure above 50 kPa, the pressure sensor exhibited its viscoelastic property. At this stage, the polymer were tightly compressed and therefore responded with a stiffer modulus of approximately 1 MPa. Overall, the deformation is well sufficient to be translated in the microfluidic structures. We further characterized the electrical resistance using a wide range of loads from 4 kPa up to 100 kPa to determine its range, linearity and sensitivity. Fig. 4b further presents the normalized electrical resistance with respect to its pressure. Similarly, we noted a linear relationship up to 50 kPa, with an *R*-squared linear fitting value of 0.993. Pressure sensitivity may be

defined by the normalized resistance per unit pressure, thus the sensor sensitivity may be measured from the slope function, approximating to 0.05 kPa^{-1}. This is a few orders more sensitive than other reported sensors of similar working pressure range,[27–29] and approximately 25 times higher than that of our previous study.[24] Furthermore, we noted that as the pressure increased above 50 kPa, the normalized resistance increased less than proportionately. Again, this correlated well with the viscoelastic effect described earlier. Due to the stiffer modulus at higher compressive load, the rate of deformation was reduced, resulting in less than proportionate increase in electrical resistance. Even so, the pressure followed a linear correlation of 0.928 and the pressure sensitivity within this range was up to 0.024 kPa^{-1}, which is well sufficient for distinguishing bodily interactions.

The robustness of liquid-based sensors has been previously demonstrated,[19,30] and they were functional even when rolled over by a car wheel.[24] To further validate our sensor, we subjected the sensor to extreme deformations, such as bending, twisting, and crushing. Fig. 4c shows the sensor under these deformations. We noted that the sensor remains intact and functional with stable electrical connectivity even after these deformations. To determine its reliability, we performed dynamic load on the microfluidic pressure sensor using a linear actuator. We subjected the sensor to cyclic loads of over 2500 cycles. Fig. 4d presents the dynamic profile of the normalized resistance of the sensor during the cyclic loads, and the inset shows the electrical profile of the sensor across a representative time scale of 200 seconds. Here, the profile was clearly consistent and highly repeatable. However, over an extended period of cyclic loading, the peak resistance decreased slightly less than 8%. This could be due to the elastic strain energy of the elastomer, which resulted in stress relaxation with cyclic loading. Despite the repeated loading, the integrity of the sensor was highly preserved, further highlighting its durability and robustness. Next, we subjected our sensor to temperature variations between 15 °C and 45 °C to observe for changes in its electrical profile. First, we cooled the sensor using ice packs. Subsequently, the sensor was mounted on an electric heater. Both the temperature and the electrical resistance of the sensor were monitored continuously. Fig. 4e shows the resistance profile of the sensor with its corresponding temperature. Evidently, the device was not affected by temperature variations. Overall, our pressure sensor is capable of measuring the force consistently over a wide range of pressures and continuously over long periods. It also remained reliable over a wide range of temperatures.

Application of pressure sensor

Object grasping is an essential task in human daily activity primarily involving the palm, index finger and thumb. The contact forces have to be sufficiently large to prevent slipping but not excessive to cause damage to the object.[31] Typically, object manipulation requires contact pressures between 2 N and 10 N.[32] This is equivalent to approximately 5 kPa to 50 kPa. As a proof-of-concept, three sensors were embedded at the following locations on the glove: distal phalange of the right index finger, right anterior trapezoid of the palm, distal phalange of the right thumb (see Fig. 5a). The sensors were located on relatively flat regions on the hand to minimize deformation induced changes due to movement or bending. We further validated this by performing hand movements, such as waving, finger bending, and pressing on the electrodes with negligible resistance changes observed. To ensure

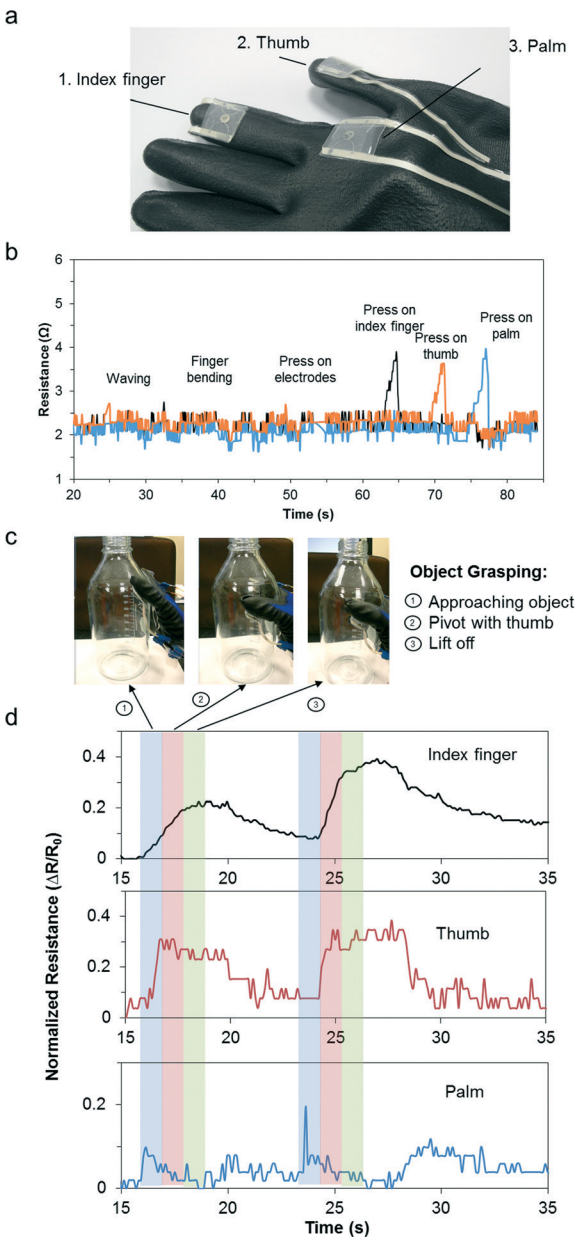

Fig. 5 Analysis of object grasping. (a) Positions of the sensors: index finger, thumb and palm region. (b) Resistance profile of the sensors during hand movements, such as waving, finger bending and pressing on electrodes. Subsequently, pressure was exerted on each sensor sequentially. (c) Actions of object grasping comprise approaching object, pivoting, and lifting object off. (d) Normalized electrical resistance change ($\Delta R/R_0$) profile of the various pressure sensors during the object grasping action.

independent pressure sensor readouts, we pressed on the individual sensors sequentially and observed distinct peaks (Fig. 5b). The subject then performed object grasping and the dynamic pressure responses were monitored simultaneously. Fig. 5c presents the actions that corresponded to object grasping actions, namely "approaching the object", "pivot with thumb", and "lift off". As shown in Fig. 5d, the hand approached the object until the palm came into contact with the device. Subsequently, the thumb flexed to form a pivot around the object. Finally, the index finger flexed fully and provided the highest grip force before the object was successfully lifted off the table. The electrical resistance readouts were consistent and repeatable. This highlights its potential as a wearable pressure sensor for real-time monitoring and analysis. In particular, a simple object grasping task may be analyzed based on the contributions from major coordinating muscle groups and could potentially be used as a rehabilitative or diagnostic medical screening tool.

Conclusions

We developed a facile method of integrating a micropatterned silicone elastomer filled with conductive fluid and bonded to a polymeric film to form a microfluidic tactile or pressure sensor with high flexibility, durability, and sensitivity. The flexible pressure sensor has sensitivity of 0.05 kPa^{-1} and is capable of distinguishing mechanical loads of between 4 kPa and 100 kPa. Furthermore, the microfluidic pressure sensor is capable of withstanding repeated loading without compromising its integrity. We believe this sensor will have great potential for use as a microfluidic wearable technology for biomedical and healthcare applications.

Acknowledgements

This research was supported by the National Research Foundation, Prime Minister's Office, Singapore under its medium-sized centre programme, Centre for Advanced 2D Materials and its Research Centre of Excellence, Mechanobiology Institute, as well as the MechanoBioEngineering Laboratory at the Department of Biomedical Engineering of the National University of Singapore. J. C. Y. acknowledges the support from Agency of Science, Technology and Research (A*STAR) Singapore for his graduate scholarship.

Notes and references

1 S. L. Swisher, M. C. Lin, A. Liao, E. J. Leeflang, Y. Khan, F. J. Pavinatto, K. Mann, A. Naujokas, D. Young, S. Roy, M. R. Harrison, A. C. Arias, V. Subramanian and M. M. Maharbiz, *Nat. Commun.*, 2015, **6**, 6575.

2 M. Chattopadhyay and D. Chakraborty, in *Next Generation Sensors and Systems*, ed. C. S. Mukhopadhyay, Springer International Publishing, Cham, 2016, pp. 143–160, DOI: 10.1007/978-3-319-21671-3_7.

3 M. Melnykowycz, M. Tschudin and F. Clemens, *Sensors*, 2016, **16**, 326.

4 S. Gong, W. Schwalb, Y. Wang, Y. Chen, Y. Tang, J. Si, B. Shirinzadeh and W. Cheng, *Nat. Commun.*, 2014, **5**, 3132.

5 S. Xu, Y. Zhang, L. Jia, K. E. Mathewson, K.-I. Jang, J. Kim, H. Fu, X. Huang, P. Chava, R. Wang, S. Bhole, L. Wang, Y. J. Na, Y. Guan, M. Flavin, Z. Han, Y. Huang and J. A. Rogers, *Science*, 2014, **344**, 70–74.

6 R. F. Shepherd, F. Ilievski, W. Choi, S. A. Morin, A. A. Stokes, A. D. Mazzeo, X. Chen, M. Wang and G. M. Whitesides, *Proc. Natl. Acad. Sci. U. S. A.*, 2011, **108**, 20400–20403.

7 S. A. Morin, R. F. Shepherd, S. W. Kwok, A. A. Stokes, A. Nemiroski and G. M. Whitesides, *Science*, 2012, **337**, 828–832.

8 C. Yeom, K. Chen, D. Kiriya, Z. Yu, G. Cho and A. Javey, *Adv. Mater.*, 2015, **27**, 1561–1566.

9 Y. Menguc, Y. L. Park, H. Pei, D. Vogt, P. M. Aubin, E. Winchell, L. Fluke, L. Stirling, R. J. Wood and C. J. Walsh, *Int. J. Robot. Res.*, 2014, **33**, 1748–1764.

10 Y. Joo, J. Byun, N. Seong, J. Ha, H. Kim, S. Kim, T. Kim, H. Im, D. Kim and Y. Hong, *Nanoscale*, 2015, **7**, 6208–6215.

11 E. Sardini, M. Serpelloni and V. Pasqui, *IEEE Trans. Instrum. Meas.*, 2015, **64**, 439–448.

12 Y. L. Park, B. R. Chen, N. O. Perez-Arancibia, D. Young, L. Stirling, R. J. Wood, E. C. Goldfield and R. Nagpal, *Bioinspiration Biomimetics*, 2014, **9**, 016007.

13 C. M. Boutry, A. Nguyen, Q. O. Lawal, A. Chortos, S. Rondeau-Gagné and Z. Bao, *Adv. Mater.*, 2015, **27**, 6954–6961.

14 Y. Hattori, L. Falgout, W. Lee, S.-Y. Jung, E. Poon, J. W. Lee, I. Na, A. Geisler, D. Sadhwani, Y. Zhang, Y. Su, X. Wang, Z. Liu, J. Xia, H. Cheng, R. C. Webb, A. P. Bonifas, P. Won, J.-W. Jeong, K.-I. Jang, Y. M. Song, B. Nardone, M. Nodzenski, J. A. Fan, Y. Huang, D. P. West, A. S. Paller, M. Alam, W.-H. Yeo and J. A. Rogers, *Adv. Healthcare Mater.*, 2014, **3**, 1597–1607.

15 J. Zhang, M. Shi, H. Chen, M. Han, Y. Song, X. Cheng and H. Zhang, *IEEE 29th International Conference on Micro Electro Mechanical Systems (MEMS)*, 2016, pp. 173–176.

16 S. Khan, S. Tinku, L. Lorenzelli and R. S. Dahiya, *IEEE Sens. J.*, 2015, **15**, 3146–3155.

17 M. Amjadi, Y. J. Yoon and I. Park, *Nanotechnology*, 2015, **26**, 375501.

18 H. Tian, Y. Shu, X.-F. Wang, M. A. Mohammad, Z. Bie, Q.-Y. Xie, C. Li, W.-T. Mi, Y. Yang and T.-L. Ren, *Sci. Rep.*, 2015, **5**, 8603.

19 Kenry, J. C. Yeo, J. Yu, M. Shang, K. P. Loh and C. T. Lim, *Small*, 2016, **12**, 1593–1604.

20 B. Zhu, Z. Niu, H. Wang, W. R. Leow, H. Wang, Y. Li, L. Zheng, J. Wei, F. Huo and X. Chen, *Small*, 2014, **10**, 3625–3631.

21 B. Nie, R. Li, J. D. Brandt and T. Pan, *Lab Chip*, 2014, **14**, 1107–1116.

22 Y. L. Park, B. R. Chen and R. J. Wood, *IEEE Sens. J.*, 2012, **12**, 2711–2718.

23 M. D. Dickey, R. C. Chiechi, R. J. Larsen, E. A. Weiss, D. A. Weitz and G. M. Whitesides, *Adv. Funct. Mater.*, 2008, **18**, 1097–1104.

24 J. C. Yeo, Kenry, J. Yu, K. P. Loh, Z. Wang and C. T. Lim, *ACS Sens.*, 2016, **1**, 543–551.
25 A. Kaneko, N. Asai and T. Kanda, *J. Hand Ther.*, 2005, **18**, 421–425.
26 H. E. Wheat, L. M. Salo and A. W. Goodwin, *J. Neurosci.*, 2004, **24**, 3394–3401.
27 A. P. Gerratt, H. O. Michaud and S. P. Lacour, *Adv. Funct. Mater.*, 2015, **25**, 2287–2295.
28 H.-B. Yao, J. Ge, C.-F. Wang, X. Wang, W. Hu, Z.-J. Zheng, Y. Ni and S.-H. Yu, *Adv. Mater.*, 2013, **25**, 6692–6698.
29 A. D. Smith, F. Niklaus, A. Paussa, S. Vaziri, A. C. Fischer, M. Sterner, F. Forsberg, A. Delin, D. Esseni, P. Palestri, M. Östling and M. C. Lemme, *Nano Lett.*, 2013, **13**, 3237–3242.
30 H. Ota, K. Chen, Y. Lin, D. Kiriya, H. Shiraki, Z. Yu, T. J. Ha and A. Javey, *Nat. Commun.*, 2014, **5**, 5032.
31 V. Iyengar, M. J. Santos, M. Ko and A. S. Aruin, *Neurorehabil. Neural Repair*, 2009, **23**, 855–861.
32 D. A. Nowak, J. Hermsdörfer and H. Topka, *J. Neurol.*, 2003, **250**, 850–860.